

## Digital image correlation in mechanical materials testing

Mikko Hokka, Amos Gilat and Veli-Tapani Kuokkala

**Summary.** Mechanical testing of materials involves measurement of stress, strain, and strain rate and typically several different techniques are used to determine strain and stress at different strain rate and temperature regimes. The techniques usually include LVDT transducers, extensometers, and strain gages. Comparison of the strains measured using these different techniques can sometimes be difficult, especially if different specimen geometries are used at different strain rate regimes. Digital image correlation combined with high speed digital cameras is an extremely effective tool that can be used to measure strains directly from the surface of the specimen by following the displacements of the high contrast speckle pattern applied on the surface of the specimen. The technique is not restricted by strain rates rather than by the technical performance of the cameras. The spatial 3D displacements and strain distributions on the surface of the specimen can be calculated from the image pairs with a very high spatial resolution even with moderate pixel resolutions of the images. This paper describes the digital image correlation procedures and shows how the technique can be used in practice to analyze tension, compression, and torsion tests at a wide range of strain rates.

*Key words:* digital image correlation, mechanical testing, Hopkinson split bar, high strain rates

### Introduction

Understanding the material behavior and knowing the material properties is important for all engineering purposes. Designing of structures and building of constitutive models to simulate the behavior of structures requires reliable material data. Also, the material and structural behavior of components and structures usually has to be characterized in a wide range of conditions for a safe and well predictable operation of machines and constructions. Therefore, materials testing has been an important part of mechanical engineering for centuries and a myriad of testing methods and techniques exists for different purposes. Often the material behavior and properties must also be known at different temperatures and loading rates in compression, tension, and torsion. In addition to these, knowing also the fatigue, corrosion, and fracture behavior of materials is important.

The material behavior at different temperatures, strain rates and loading conditions can vary significantly. The strength of most crystalline metals increases with increasing strain rate and decreasing temperature. Also the ductility, strain hardening rate, and fracture toughness are usually affected by strain rate and temperature. At low and intermediate strain rates ( $<500 \text{ s}^{-1}$ ) the strength typically increases linearly with respect to the logarithm of strain rate. The material behavior at these conditions is usually explained by the thermally activated dislocation motion: at higher temperatures the dislocations

have more thermal energy to overcome the glide obstacles on the glide planes, and at lower strain rates they have more time to wait for a suitable energy boost with high enough amplitude to help them overcome the obstacles. At higher strain rates the behavior changes significantly and the strength increases more rapidly than predicted by the thermal activation concept. The dislocation motion is now controlled by several drag mechanisms that consume more energy that can only be supplied by the externally applied force. For most metals, the mechanisms change at strain rates around  $10^3 \text{ s}^{-1}$ , which is seen as an upturn in the strength vs. logarithmic strain rate plot.

Materials testing, such as compression, tension, and torsion testing, can be carried out at a wide range of strain rates and temperatures. Low rate experiments are typically carried out with servohydraulic materials testing machines that can also be equipped with high and low temperature capabilities. For intermediate strain rates, there are several possibilities such as high velocity hydraulic actuators, drop towers, cam-plastometers, and recently developed intermediate strain rate Hopkinson Bar devices [1]. The conventional Hopkinson Bar devices are used to characterize the material behavior at even higher strain rates, and explosive driven impact tests are utilized in the highest strain rate regime.

The measurement techniques used at different temperature and strain rate regimes and for different loading vary. At low strain rates the force acting on the specimen is usually measured simply with an axial and/or angular load cell that is connected in series with the specimen and the load frame. The strain, in turn, can be measured using linear variable differential transducers or with an extensometer attached directly to the specimen. At higher strain rates, the load cannot be measured using a simple load cell, because the load is applied by a rapidly increasing stress pulse that reverberates in the load cell causing severe oscillations in the measured signal. Also measurement of strain with an extensometer at high strain rates is practically impossible due to the small size of the specimens and the limited dynamic properties of the extensometers. Therefore, specimen force and strain are usually indirectly measured from the pressure bars, where the stress pulses can be recorded provided the bars are long enough and the reflections of the pulses from the ends of the bars do not overlap with the measurement signal. The stress pulses are usually measured using strain gages bonded on the surfaces of the stress bars. The time resolved stress, strain, and strain rate can be calculated from the measured stress pulses. However, the comparison of results obtained at different strain rate regimes can sometimes be difficult, especially if different specimen geometries are used in the low and high strain rate tests.

The specimens in high rate testing are limited in size by the need to reach force equilibrium within the first few percent of strain. Therefore, the strain is usually calculated from the displacements of the ends of the specimen or stress bars by assuming a simple shear, uniaxial compression, or tensile state of stress. The stress state in compression usually is close to uniaxial, at least for small and moderate strains, and the strains measured from the displacements of the ends of the push rods are quite accurate [2]. In tension, however, the stress state is more complex especially in the fillet areas of the dog bone shaped specimen. Typically, the specimen yields also in the fillets, and all this contributes to the strain determined from the movements of the ends of the specimen or the stress bars. As a consequence, the strains measured in tension tests can differ significantly from the true strains in the specimen gage section. Previously, the effect of

specimen geometry on the tension test results has been studied by several authors. Verleysen and Degrieg [12-14] extensively studied the effect of specimen geometry in tension using rotating drum cameras to measure the axial strain distributions in high rate tests. According to their work, the strains measured before necking from the displacements of the bars tend to overestimate the true strains in the specimen due to the yielding of the fillet areas. Similar findings were presented by Curtze et al. [15]. Also, in both tension and torsion tests the strain typically localizes at some point during the test, which is usually followed by plastic instability, necking, or formation of a localized shear band, and failure of the specimen. The strain measured from the displacements of the ends of the bars or the specimen does not take into account the locally higher strains in the necking/shearing region that can be significantly higher than elsewhere in the specimen. The true stress calculated by assuming uniform reduction of the original cross section of the gage length does not either take into account the locally smaller cross sectional area in the localized region. Therefore, the values of both the average strain and average stress can be significant underestimations of the true strain and true stress in the localized region.

One of the methods that has been developed to overcome these limitations is the Digital Image Correlation (DIC) technique. Digital image correlation enables non-contact measurement of the strains on the surface of the specimen during the test at a very wide range of strain rates. The technique is based on recording a series of images of the specimen during the deformation with digital cameras and calculating the surface displacements from these images. The technique can be used with only one camera (2D) for planar strain analysis, or with two cameras (3D) that allow the determination of the full field strains during the test. The surface strains can be determined with a very high spatial resolution, and the applicable strain rate range is only limited by the image acquisition rate, optical capabilities, and resolution of the digital camera(s).

Digital image correlation consists of several steps that include recording the measurement data in the form of digital images, algorithms to analyze the data contained in the images, and automating the procedures. Today, very sophisticated software are available that combine all necessary steps and algorithms for reliable and accurate image correlation. The software basically needs to be able to transfer the real 3D coordinates of the specimen surface to the 2D image plane coordinate system, then combine the data from the two cameras, and reconstruct the digital 3D image of the surface of the specimen. This is usually done by applying a simple pinhole projection model and by correcting for the lens distortions and other experimental errors by calibrating the model with a known target pattern. The most important feature of the digital image correlation software is the pattern recognition capability, which starts from the reference image pair and works through all consecutive image pairs to calculate the 3D coordinates of the specimen surface in the deformed configurations. The pattern recognition cannot usually be done for individual pixels, but instead small groups of pixels or image subsets are used to identify the coordinates from each image pair. In 3D image matching, the same pattern must be recognized from both images of the pair in order to calculate the current coordinates of the surface points. Therefore, the cameras must be synchronized to take the images at the same moment of time, and also the pixel-to-pixel correspondence of the images must be close enough for successful pattern matching. In practise, the cameras must be aligned so that each pixel in both images corresponds to the same spot on the

surface of the specimen. The algorithms used for image matching are complex and include subset shape functions that enable matching of the image subsets after deformation and interpolation of the coordinates between the subsets. The interpolation of coordinates can be done with very high spatial resolution up to 1/200 pixel. For a good overview on digital image correlation, the reader is referred, for example, to [3]. In the present paper, we demonstrate the application of digital image correlation to the mechanical testing of materials and explain the benefits of the technique with examples from tests performed on ultrafine grained metals.

## **Experimental techniques**

The work presented in this paper was carried out at the Mechanical Engineering Department of The Ohio State University. Mechanical testing was done in tension, compression, and torsion at strain rates ranging from  $10^{-4} \text{ s}^{-1}$  to  $2000 \text{ s}^{-1}$ . The studied materials were severe plastic deformation processed ultrafine grained (UFG) 1070 commercially pure (99.7 wt-% Al) aluminum and near UFG AZ31 magnesium alloy. The tests were monitored using two digital cameras, and the strains on the surface of the specimen were calculated using the digital image correlation technique.

### *Digital Image Correlation*

At low strain rates ( $<1 \text{ s}^{-1}$ ), two Point Gray Research Grasshopper two megapixel cameras were used to obtain the image pairs. The cameras were operated at frame rates ranging from  $0.067 \text{ s}^{-1}$  to  $19 \text{ s}^{-1}$  depending on the strain rate, yielding an average of 200-400 image pairs per test. At strain rates  $1 \text{ s}^{-1}$  and above, two Photron Fastcam SA1.1 high speed cameras were used in the compression and torsion tests, and Photron APX RS high speed cameras in the tension tests. The frame rates for the high strain rate tests were selected so that the total number of image pairs was in the same range as for the low rate experiments. With the high speed cameras, the resolution of the images changes from 1 megapixel at the frame rate of  $10.000 \text{ s}^{-1}$  to  $192*144$  pixels at the frame rate of  $120.000 \text{ s}^{-1}$ .

The quality of the speckle pattern used in the measurements must be very good and the contrast should be maximized for maximum spatial resolution. Also, when using the 3D image correlation, recognition of the same pattern in both images is much easier with high quality high contrast patterns. The contrast pattern must be random to avoid correspondence and aperture problems that occur if one image subset can be matched to several patterns in the following images. Also, the size of one contrast dot or speckle has to be larger than a single pixel in the image, and therefore the size of the dots must be adjusted when changing the pixel resolution of the cameras.

In the tension tests discussed in this paper, the contrast pattern was applied simply by using a black permanent marker over white base coat, whereas in the torsion and compression tests the black contrast pattern was spray painted over the white background. At low strain and frame rates, the high resolution of the images allowed using a of fine pattern, which is easier to apply. Also the lighting at low strain rates can be applied simply by using regular spot lights that are aligned so that no excess glare

from the specimen to the cameras occurs and the lighting is even over the whole surface of the specimen.

At higher strain rates, the shutter time becomes shorter and the need for light increases. Therefore, two to four high intensity fiber optic lights were used to illuminate the specimen in the high rate experiments. The fiber optic lights produce a very high intensity light radiation, and the possibility of excess glare increases significantly. Also, the resolution of the cameras decreases quickly at higher frame rates. Therefore, the contrast patterns in the high strain rate compression and tension tests were hand painted either by using a black permanent marker over white base coat (tension) or with a white paint using a single bristle over a black non-glossy satin paint. The black base coat with white pattern gave the highest contrast of all patterns, and the black base coat also removed all glare. However, the pattern did not stay on the surface very well at high strains because of the high thickness of the paint layer, and in the torsion tests the contrast pattern chipped off from the surface at strains higher than 30-40 percent. Therefore, in the torsion tests the black pattern was spray painted over white base coat, which had much higher adhesion to the surface, allowing testing up to 50-80 percent of strain. Figure 1 shows examples of the contrast patterns used in the tests at different strain rates.

The strains in the specimens were calculated from the image correlation results. In the compression tests, the average engineering strain was calculated from the spatial

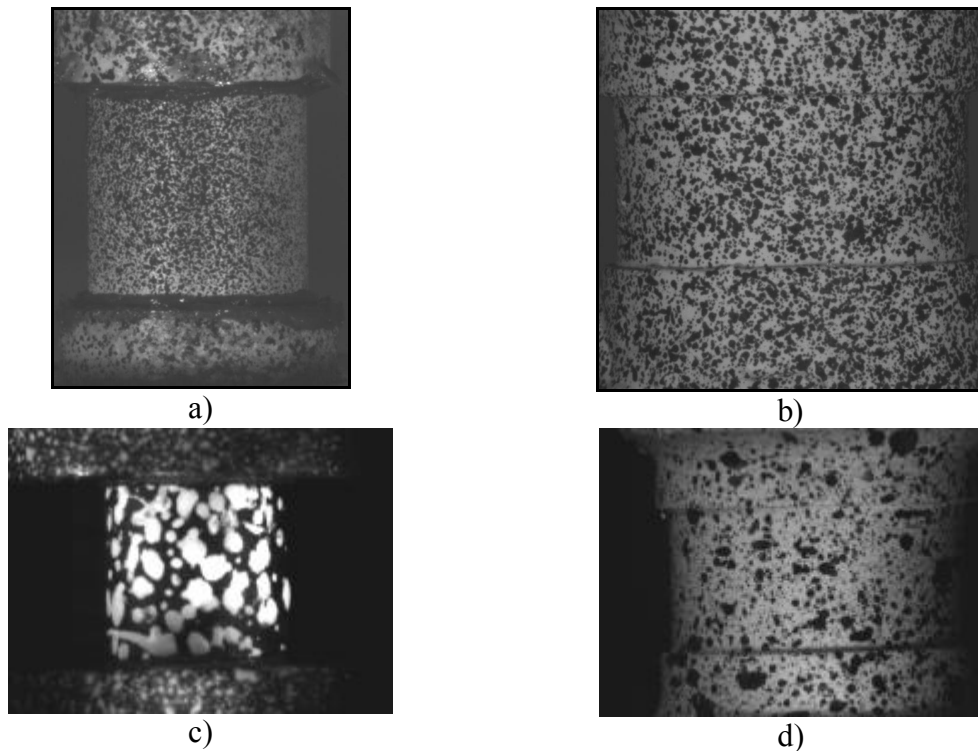


Figure 1. Examples of speckle patterns used at different strain rates; a) low rate compression tests, b) low rate torsion tests, c) high rate compression tests, and d) high rate torsion tests.

Lagrange strains measured from the surface of the specimen using Equation 1, where  $E_i$  are the spatial Lagrange strains in the tangential direction of the specimen surface. In the torsion tests, the strains on the specimen were calculated from the rotational displacements of the ends of the specimen using Equation 2, where  $\theta$  is the angle of twist between the ends of the specimen and  $\bar{a}$  and  $\bar{b}$  the vectors from the center axis of the specimen to the surface of the grip section. In the torsion tests the strain was also calculated from the Lagrange surface strains using the relation  $\gamma = \frac{1}{2}\epsilon_{xy}$ . Technical strain,  $\epsilon^T$ , was used in the tension tests, which was calculated from the elongation of an infinitesimal line element using Equation 3, where  $l$  is the length of the line in the undeformed configuration and  $l+dl$  is the corresponding length in the deformed configuration.

$$\epsilon_E = \frac{\sum_{i=1}^N \sqrt{1 + 2E_{11}^i} - 1}{N} \quad (1)$$

$$\gamma = \frac{r_s \theta}{l_s} = \frac{r_s}{l_s} \arccos\left(\frac{\bar{a} \cdot \bar{b}}{\|\bar{a}\| * \|\bar{b}\|}\right) \quad (2)$$

$$\epsilon^T = \lim_{l \rightarrow 0} \left( \frac{l + dl}{l} \right) - 1 \quad (3)$$

### *Hopkinson Split Bar Techniques*

The low rate testing was done with a conventional materials testing machine and the high rate tests using the Hopkinson Split Bar techniques. In compression the Hopkinson equipment is fairly simple, in this case consisting basically of two high strength titanium alloy pressure bars half inch in diameter. The small cylindrical specimen is sandwiched between the bars. A third bar, the striker bar, is impacted at the free end of the incident bar to create a compressive stress pulse that propagates in the incident bar towards the specimen. As the stress pulse reaches the specimen, part of it is reflected back as a wave of tension while a part of it is transmitted through the specimen into the transmitted bar. As the wave travels through the specimen, the specimen undergoes dynamic elastoplastic deformation at a high rate. The displacements of the ends of the bars and the time resolved force history of the bars can be calculated from the three stress pulses; incident, reflected, and transmitted that are measured with strain gages bonded on the surfaces of the bars, amplified, and recorded on a digital oscilloscope. From these signals, the strain, strain rate, and stress in the specimen can be calculated as a function of time using equations (4)-(6). In Equations (4)-(6),  $C_0$  is the longitudinal wave velocity in the bar,  $L_s$  is the gage length of the specimen,  $A_b$  is the diameter of the stress bar,  $E$  is the Young's modulus of the stress bar,  $A_s$  the cross sectional area of the specimen, and  $\epsilon_r$  and  $\epsilon_t$  are the reflected and transmitted strain pulses measured with strain gages from the bars. A schematic picture of a compression Hopkinson Split Bar device is shown in Figure 2.

$$\dot{\epsilon} = \frac{2C_0 \epsilon_r(t)}{L_s} \quad (4)$$

$$\epsilon(t) = \frac{2C_0}{L_s} \int_0^t \epsilon_r(t) dt \quad (5)$$

$$\sigma(t) = \frac{A_b E \epsilon_t(t)}{A_s} \quad (6)$$

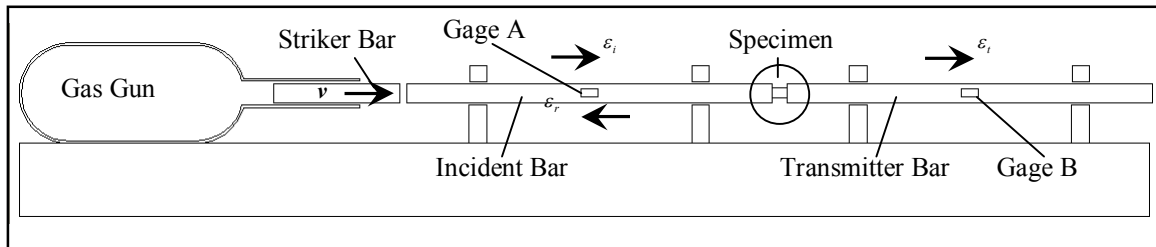


Figure 2. Schematic picture of a compression Hopkinson Split Bar device.

The tension and torsion Hopkinson Split Bar devices are more complex than the compression bar. The incident tension or torsion pulse cannot be created simply by impacting the striker bar at the free end of the incident bar. Also, the specimen has to be properly fixed to the ends of the bars. There are several methods that can be used to create the incident tension pulse, such as impacting a tubular striker at a flange machined to the free end of the incident bar. Both mechanical fixing and gluing are used to fix the specimen to the bars. In this work, both the tension and torsion incident pulses were created by first clamping the incident bar at a suitable position, storing the load into its free end by a hydraulic pulley, and then suddenly releasing the stored load/torque by breaking the brittle clamp pin with a second hydraulic press. The specimen was fixed to the stress bars by gluing it to special adaptors, which were then further glued to the ends of the stress bars. A schematic picture of the torsion setup is shown in Figure 3, and a general view of the tension and torsion devices is shown in Figure 4.

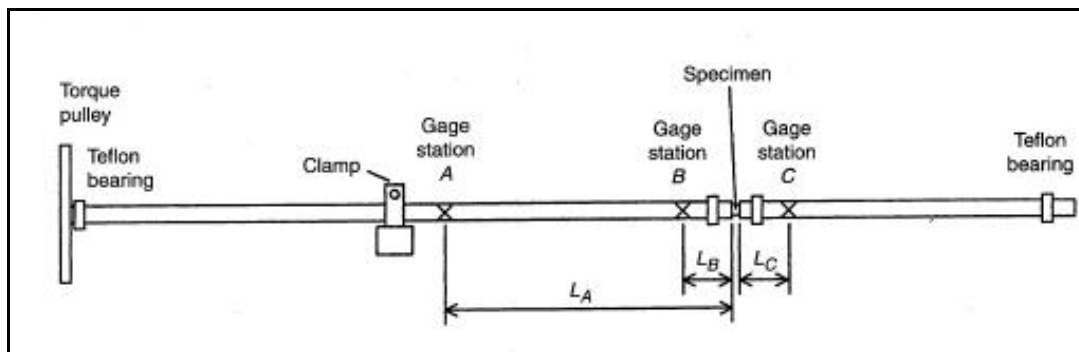


Figure 3. A schematic picture of a torsion Split Hopkinson Pressure bar device [4].

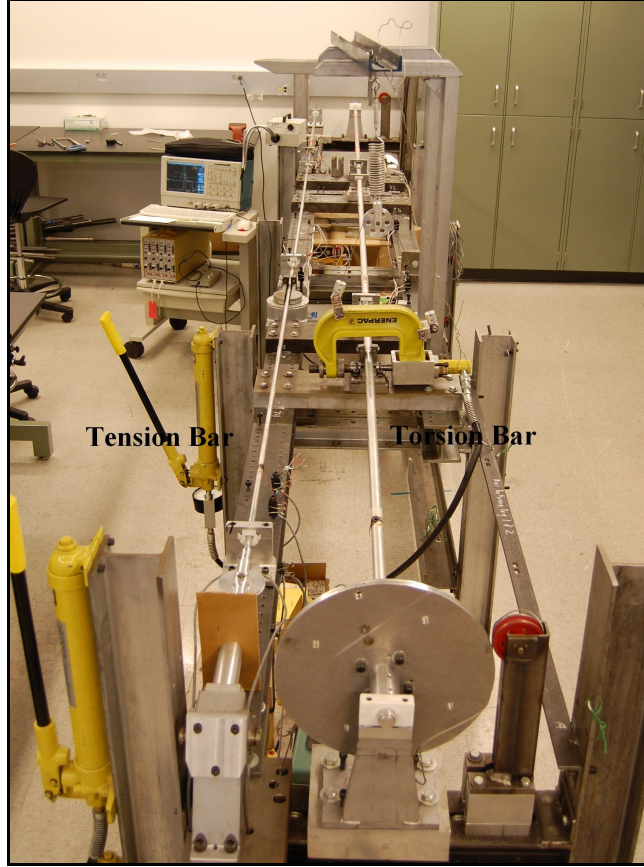


Figure 4. Tension and torsion bar setups at the Department of Mechanical Engineering of The Ohio State University.

In these setups, the incident bar has two strain gage stations, and the reflected pulse is calculated from the measured pulses by applying appropriate time shifts [4]. The strain rate in the tension and torsion tests was calculated using Equations (7) and (8), and the strain simply by integrating the strain rate over time. Shear stress is calculated using Equation (9). In Equations (7)-(9),  $c$  is the shear wave speed in the bar,  $L_s$  is the gage length of the specimen,  $r_s$  and  $r_b$  are the radii of the specimen and the stress bar,  $t_s$  is the average wall thickness of the torsion specimen, and the strains  $\epsilon$  and  $\gamma$  are the strain gage signals measured at strain gage stations a, b and c.  $t_s$  is the transmitted torque, and the time shifts  $t_a$ ,  $t_b$  and  $t_c$  are the distances in time that the pulse travels from the respective strain gage station to the specimen or from the specimen to the strain gage station, i.e.,  $t_a=L_a/c$  etc.

$$\dot{\epsilon} = \frac{c}{L_s} [\epsilon_a(t-t_a) + \epsilon_a(t-t_a-2t_b) - \epsilon_b(t-t_b) - \epsilon_c(t-t_c)] \quad (7)$$

$$\dot{\gamma} = \frac{c}{L_s} \frac{r_s}{r_b} [\gamma_a(t-t_a) + \gamma_a(t-t_a-2t_b) - \gamma_b(t-t_b) - \gamma_c(t-t_c)] \quad (8)$$

$$\tau = \frac{T_t}{2 \pi r_s^2 t_s} \quad (9)$$

### *Materials*

The results shown in this paper are from tests performed on an ECAP processed ultrafine grained 1070 (99.7-wt% Al) aluminum and a reciprocating extrusion processed near ultrafine grained AZ31 magnesium alloy. Tension and torsion tests were performed on the ultrafine grained 1070 aluminum alloy and compression tests on the near UFG AZ31 magnesium alloy. Also a few torsion tests were performed on a standard 7075-T6 aluminum alloy for comparison. For a full description of the materials, tests and discussions of the results, see refs. [5-11]

### **Discussion and examples of the results**

Materials testing at very high strain rates is complicated by several scientific and practical challenges. One of the most difficult tasks to conduct at high rates is accurate measurement of strain, which is usually done by assuming that the stress state is uniaxial and the deformation is confined to a well defined gage length. In most cases neither of these assumptions is exactly true, and especially the strains measured in high rate tension and torsion tests can be markedly erroneous. Also, in tension tests the true strain and true stress can only be calculated until the start of necking of the specimen. The following Chapter demonstrates with examples how digital image correlation can be used to overcome these problems.

#### *Tension testing*

In the high rate tension tests, the strain calculated from the stress pulses measured from the bars is based on the assumption that the specimen only yields inside the gage section and that the deformation is uniform until the final fracture of the specimen. Therefore, any kind of localization of strain is not taken into account, and the strain after commencing of necking can contain significant errors. Figure 5 shows typical dog bone shape specimens used in the tensile tests. For the UFG 1070 aluminum, the gage length was only 6 mm, the width 4 mm, and the thickness 2 mm. The black horizontal lines plotted in Figure 5 are the lines along which the waterfall plots shown in Figure 6 are plotted. The red diamond shows the location of maximum axial strain.

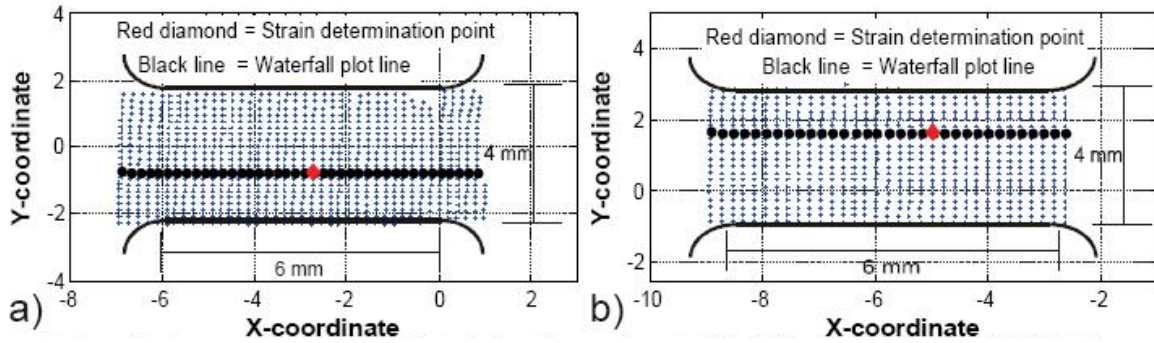


Figure 5. Coordinate maps for the tension specimens and locations of the maximum strain and the paths along which the waterfall plots in Figure 6 were plotted, a) a specimen tested at an average strain rate of  $1500 \text{ s}^{-1}$  and b) a specimen tested at an average strain rate of  $350 \text{ s}^{-1}$  [10].

Figure 6 shows the waterfall plots determined from the tension tests performed at strain rates  $1500 \text{ s}^{-1}$  and  $350 \text{ s}^{-1}$  for the UFG 1070 aluminum. The strain localization starts very rapidly after the initial yielding at both strain rates. This is consistent with the engineering stress strain curves typically measured for the nanocrystalline and ultrafine grained metals. The localization continues throughout the tests, and the maximum strains are located in the necking region. From the waterfall plots it is clear that also the shoulder regions of the specimens yield, and axial strain between 3 and 8 percent can be observed for both specimens. The inhomogeneous deformation gradually leads to increasing stress triaxiality instead of the assumed one dimensional stress state. Also, the strains, stresses, and strain rates are much higher in the necking region than the average values measured for the whole cross section and gage length. Therefore, the stress strain curves calculated from the average values do not represent the material behavior correctly after necking.

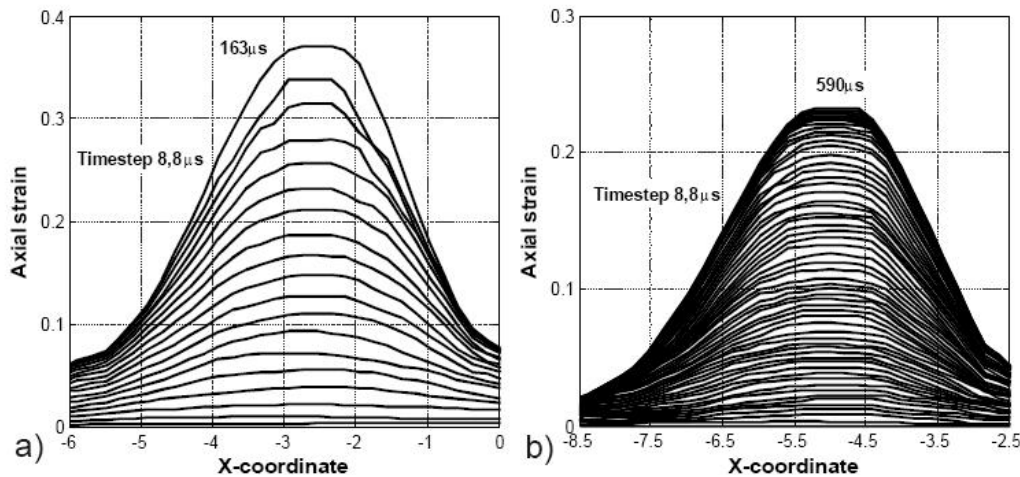


Figure 6. Axial strains along the gage length at 8.8 microsecond time intervals a) for a specimen tested at an average strain rate of  $1500 \text{ s}^{-1}$ , and b) for a specimen tested at an average strain rate of  $350 \text{ s}^{-1}$  [10].

The true stress in the tensile test can be calculated with the commonly used equations only until the necking starts. However, with DIC the true cross sectional area of the

specimen also in the necking region can be calculated either by assuming constant volume, i.e.,  $dV=0$ , or by measuring the actual strain in the specimen also in the Z-direction and then assuming that the relative strain rate is the same in the Z-direction as in the axial and transverse directions. Figure 7 shows a comparison of the different stress - strain curves that can be obtained from the tension test. The gray solid line is the original Hopkinson Split Bar data, where the engineering stress and strain are calculated from the bar stresses. The dashed black line represents the engineering stress strain curve, where the strain is determined with DIC. The strain used in the plot is determined from the point marked in Fig. 5a. The solid and dotted black lines are the true stress – true strain curves, where the cross sectional area of the specimen is determined from the actual strain measurement and by assuming constant volume. From the plot it is clear that the true stress - true strain curves are at significantly higher stress levels than the engineering curves simply because of the rapidly reducing cross sectional area of the neck. In addition, the true stress – true strain curves show a clearly positive strain hardening rate, which is not obvious from the engineering values. It should, however, be noted that the stress triaxiality gradually increases during necking, and in the present analysis this is not taken into account. Nevertheless, at least for moderate levels of necking the stresses calculated in the described manner can be assumed to represent the real true stresses in the neck area quite well.

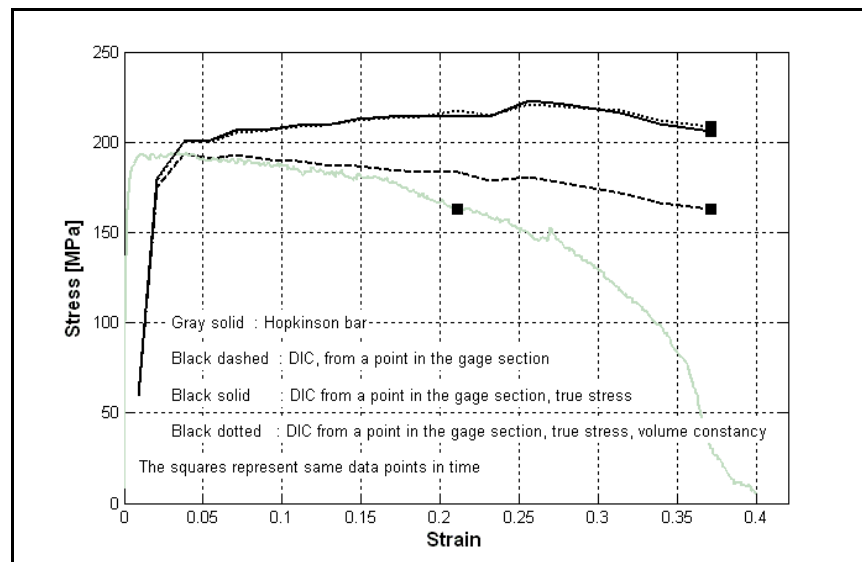


Figure 7. Stress-strain curves with different strain and stress determinations for the ultrafine grained 1070 aluminum at the strain rate of  $1500 \text{ s}^{-1}$  [after 10].

### *Torsion testing*

The strains determined in the torsion tests are shown in Figure 8. The shear strain calculated from the Lagrange shear strain ( $\gamma=2*\epsilon_{xy}$ ) shows higher values than the shear strain calculated from the displacements of the ends of the bars (Eq.2) and from the strain gage signals for both 7075-T6 (Fig. 8a) and UFG 1070 (Fig. 8b). The shear strains obtained from the displacements of the ends of the bars (Eq.2) and from the stress pulses measured from the bars are closer to one another. The difference between the strains can

be simply explained by the localization of strain, which is not taken into account in the average strains calculated from the stress pulses or obtained with Eq. 2 for the whole gage section. The average Lagrange strain, on the other hand, is calculated directly from the gage section and includes also the high strains in the shear band. However, even the Lagrange strain does not correspond to the maximum strain in the localized shear band, which is still higher than the spatial average strain in the gage section. The average shear strains in the specimen calculated from the rotational displacements of the ends of the bars (Eq.2) and from the stress pulses differ mainly because of the slightly eccentric motion of the bars and the specimen. In addition, the axial and transverse strains in the specimen that are not taken into account by the one dimensional theory of wave motion that is applied in the calculation of the specimen strain from the stress pulses in the bars. As seen in Figure 8, the Lagrange strains in the axial ( $\epsilon_{yy}$ ) and the transverse ( $\epsilon_{xx}$ ) directions are clearly non-zero, i.e., the deformation is not simple shear.

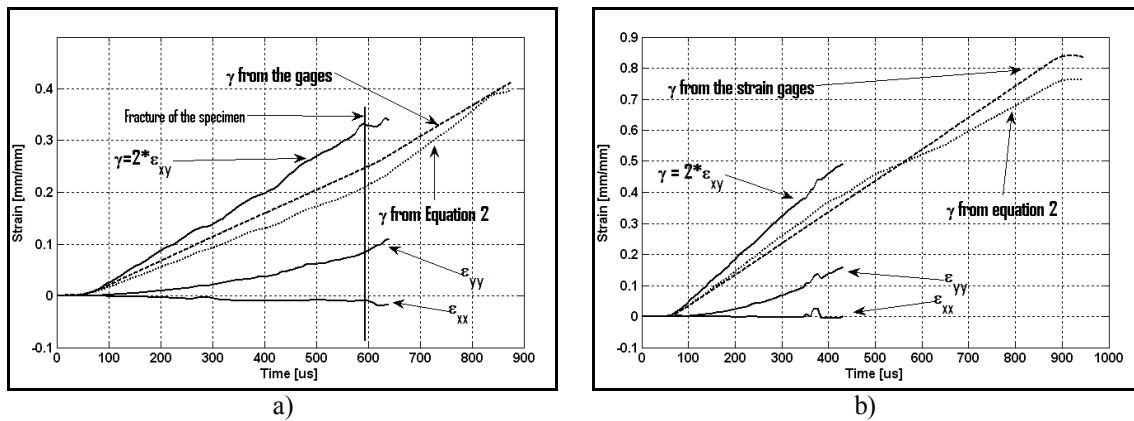


Figure 8. Shear strains measured during a dynamic torsion test for a) 7075-T6 aluminum alloy and b) UFG 1070 aluminum [7].

The shear stress - shear strain curves obtained with different strain determinations are shown in Figure 9. The specimens did not fail during the tests and therefore the drop of stress at the end of the test does not represent failure but only marks the end of the experiment. As seen in Figure 9, at the end of the test the shear strain calculated from the stress waves measured from the bars is about 8% higher than the strain obtained from the displacements of the specimen ends using DIC. In the torsion tests, the stress does not depend on the strain or its localization unless there is a significant axial strain component that leads to changes in the wall thickness of the specimen during the experiment.

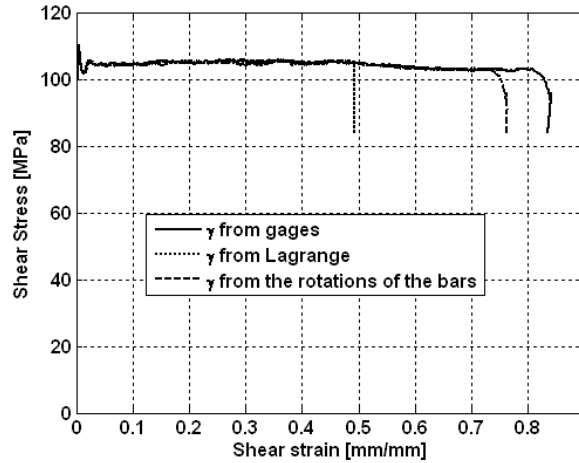


Figure 9. The shear stress - strain curves obtained with different strain determinations for the ultrafine grained 1070 aluminum tested at the strain rate of  $1000 \text{ s}^{-1}$  [7].

Figure 10 shows the localization of shear in the torsion tests. Figure 10a is a waterfall plot of the shear strain calculated from the Lagrange shear strain ( $\gamma=2\epsilon_{xy}$ ) along the gage length of the specimen. The localization of strain starts very rapidly after yielding and continues throughout the test. The maximum strain at the time when the contrast pattern chips off from the specimen surface is already more than 45 percent, while the right hand side of the specimen shows only about 22% and the left hand side as little as 5 % of strain. Figure 10b shows a fully developed shear band after a significant amount of strain. The maximum strains in the shear band are around 50 percent, and the width of the shear band is of the order of one millimeter. The strain immediately outside the shear band is roughly half of that, and the ends of the gage section are almost undeformed.

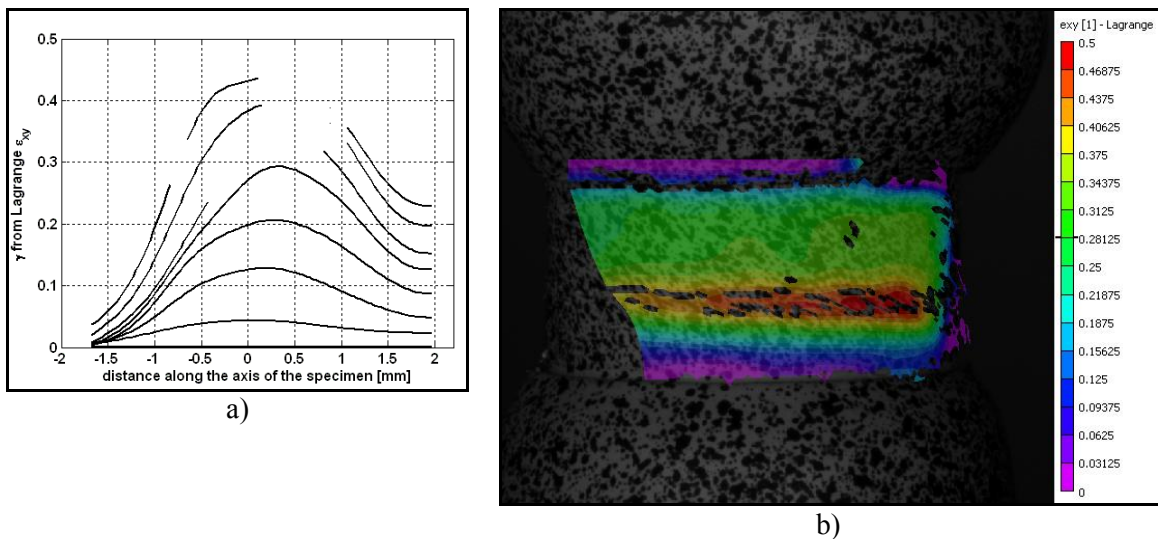


Figure 10. Shear band formation in the torsion test of UFG 1070 aluminum a) waterfall plot along the gage section of the specimen [7] and b) fully developed shear band in the middle of the gage length [8].

## Compression testing

The stress - strain curves obtained from quasi-static compression tests using different strain determinations are compared in Figure 11. The average strains calculated from the displacements of the anvils are very close to those determined from the surface of the specimen using Equation (1), both strains being determined with the digital image correlation technique. In the beginning of the test the strains are almost identical, but at larger deformations the strains measured from the anvil displacements show slightly higher values. This is typical for compression tests, where the specimen tends to barrel at larger deformations leading to lower tangential strains on the surface of the specimen. However, for a material such as the near ultrafine grained AZ31, for which the fracture strains and thus the barrelling of the specimen are relatively low, the average strains measured from the displacements of the anvils are quite close to those measured directly from the surface of the specimen.

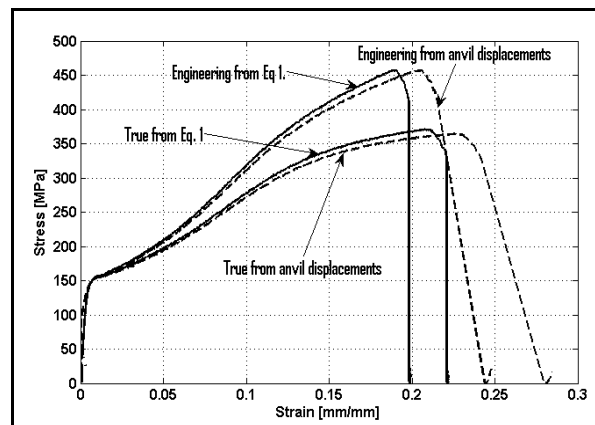
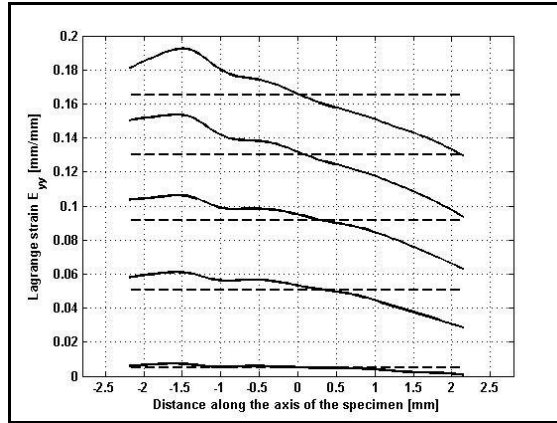
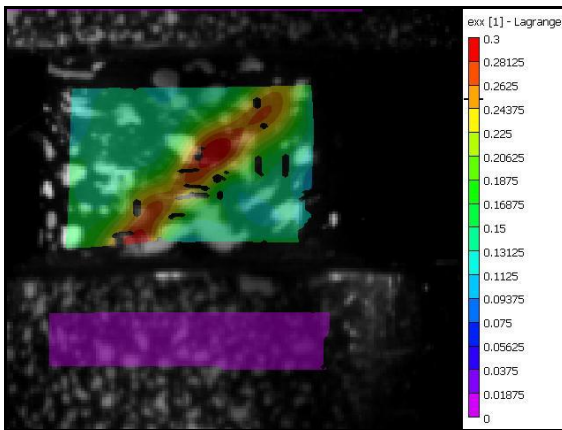


Figure 11. Stress strain curves obtained with different strain determinations for the cast, extruded, and SPD processed AZ31 in compression at the strain rate of  $10^{-3} \text{ s}^{-1}$  [9].

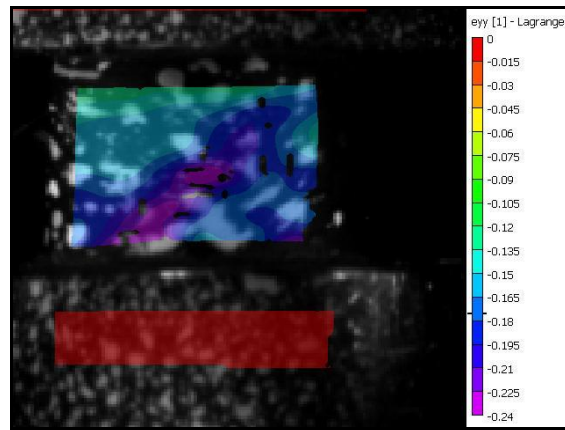
Waterfall plots for a compression test on the near UFG AZ31 magnesium alloy are shown in Figure 12a. The spatial Lagrange strain distributions along the axis of the specimen are more even when compared to the torsion and tension tests. For this specimen the strains are somewhat asymmetric with respect to position but increase quite uniformly with time. The largest difference between the maximum and minimum strains is around 7 percent. Strain localization in the specimen does not occur until just before the final fracture. The last image before fracture is shown in Figures 12b and 12c, where the Lagrange strains in the axial and transverse directions are shown over the gage section of the specimen. The fracture occurs at a 45 degree angle along the formed shear band.



a)



b)



c)

Figure 12: Distribution and localization of strain in the compression test on the cast, extruded, and SPD processed AZ31 at the strain rate of  $1000 \text{ s}^{-1}$ : a) axial strains along the gage section with average strains (dashed lines), and last frame before fracture with b) Lagrange  $\epsilon_{xx}$  (transverse strains) and c) Lagrange  $\epsilon_{yy}$  (axial strains) [9].

## Summary

Digital image correlation is an effective non-contact method for accurate strain measurements. Combined with high speed digital cameras, the technique can be used to measure 3D surface displacements and strains even at high deformation rates. In this paper, we have described how DIC can be applied to materials testing in a wide range of strain rates in tension, torsion, and compression. In tension tests with the Hopkinson Split Bar method, DIC yields more accurate strain data from the specimen gage section than can be obtained by the conventional calculations based on the displacement data of the ends of the pressure bars. The strains measured with DIC can also be used to calculate the local true stresses and strains even after the onset necking.

In a Hopkinson Split Bar torsion tests on pure 1070 UFG aluminum the material shows almost immediate localization of strain, the local strains measured on the surface

of the specimen being significantly higher than the average strains measured from the rotational displacements of the pressure bars.

In the compression the distribution of strain in the specimen was, however, found to be more uniform than in the tension and torsion tests. The fracture of AZ31 magnesium alloy specimens was preceded by a formation of a shear band at a 45 degree angle with respect to the loading direction. Also the rapid formation of the shear band could be recorded with digital image correlation technique.

## References

- [1] A. Gilat, T. Matrka, A new compressive intermediate strain rate testing apparatus, *in the proceedings of the SEM annual conference*, Indianapolis, 2010.
- [2] A. Gilat, T. Schmidt, A. Walker, Full field strain measurements in compression and tension Split Hopkinson Bar experiments, *Experimental Mechanics*, 49:291-302, 2009.
- [3] M. Sutton, J.-J. Orteu, H. Schreier, *Image Correlation for Shape, Motion, and Deformation Measurements*. Springer Science, New York, 2009.
- [4] A. Gilat, Torsional Kolsky bar testing. *ASM handbook, 8, Mechanical Testing and Evaluation*, ASM International, Materials Park, OH, USA, 2000.
- [5] A. Rosochowski, L. Oljenik, Numerical and physical modeling of plastic deformation in 2-turn equal channel angular extrusion, *Journal of Materials Processing Technology*, 125-126:309-316, 2002.
- [6] L. Oljenik, A. Rosochowski, Methods of fabricating metals from nano-technology *Bulleting of the Polish Academy of Sciences*, 53:413-423, 2005.
- [7] M. Hokka, J. Seidt, T. Matrka, A. Gilat, V.-T. Kuokkala, J. Kokkonen, S. Müller, Characterization of the mechanical behavior of ultrafine grained metals using digital image correlation, *in the proceedings of the ICEM14 international conference on experimental mechanics*, Poitiers, France, 2010.
- [8] M. Hokka, J. Kokkonen, J. Seidt, T. Matrka, A. Gilat, V.-T. Kuokkala, Dynamic torsion properties of Ultrafine Grained Aluminum, *in the proceedings of the SEM annual conference*, Indianapolis, 2010.
- [9] M. Hokka, J. Seidt, T. Matrka, A. Gilat, V.-T. Kuokkala, J. Nykänen, S. Müller, Compression behavior of near-UFG AZ31 Mg-Alloy at high strain rates, *in the proceedings of the SEM annual conference*, Indianapolis, IN, USA, 2010.
- [10] J. Kokkonen, V.-T. Kuokkala, J. Seidt, A. Walker, A. Gilat, L. Oljenik, A. Rosochowski, High strain rate deformation analysis of UFG aluminum sheet samples, *in the proceedings of the Annual SEM conference*, Albuquerque, NM, USA, 2009.
- [11] J. Kokkonen, V.-T. Kuokkala, Lech Olejnik, A. Rosochowski, Dynamic behavior of ECAP processed aluminum at room and sub-zero temperatures, *in the proceedings of the Annual SEM conference*, Orlando, FL, USA, 2008.
- [12] P. Verleysen, J. Degrieck, Optical measurements of the specimen deformation at high strain rate, *Experimental Mechanics*, 44, 2004.
- [13] P. Verleysen, J. Degrieck, Experimental investigation of the deformation of Hopkinson Bar specimens, *International Journal of Impact Engineering*, 30, 2004.

- [14] P. Verleysen, J. Degrieck, Measurement of the evolution of the axial strain distribution in Hopkinson specimens. *Journal de Physique IV*, 110, 1993.
- [15] S. Curtze, M. Hokka, V.-T. Kuokkala, T. Vuoristo, Experimental analysis on the influence of the specimen geometry on the tensile Hopkinson Split Bar test result of steel sheet, *In the proceedings of the MS&T conference*, Cincinnati, OH, USA, 2006.

Mikko Hokka, Veli-Tapani Kuokkala  
Tampere University of Technology, Department of Materials Science  
POB 589, 33101 Tampere  
mikko.hokka@tut.fi

Amos Gilat, Mikko Hokka  
The Ohio State University, Department of Mechanical Engineering  
209 W 19<sup>th</sup> Avenue, Columbus, OH 43210, U.S.A.  
gilat.1@osu.edu